J. Fluid Mech. (1999), *vol.* 381, *pp.* 175–198. Printed in the United Kingdom

Gravitational settling of particles through density interfaces

By A. N. SRDIĆ-MITROVIĆ[1], N. A. MOHAMED[2] AND H. J. S. FERNANDO[1]†

[1]Environmental Fluid Dynamics Program, Department of Mechanical and Aerospace Engineering, Arizona State University, Tempe, AZ, 85287-9809, USA

[2]Department of Power and Energy Engineering, Faculty of Engineering and Technology, Minia University, Minia, Egypt

(Received 12 February 1998 and in revised form 17 September 1998)

Gravitational settling of dense particles through density interfaces is common in many environmental and engineering flow situations, yet very little research has been done to understand the mechanics of particle–stratification interactions. To this end, a detailed experimental study was carried out to investigate the settling of solid spherical particles through density interfaces. In these experiments, the solid particles first descended through a deep homogeneous layer, entered a thick pycnocline and then descended to another denser homogeneous layer. It was found that the stratification has a significant impact on the settling of particles in the approximate parameter range $1.5 < Re_1 < 15$, where $Re_1 = U_1 d_p/\nu$ is the Reynolds number based on the particle entry velocity U_1 to the stratified layer, d_p is the particle diameter and ν is the kinematic viscosity of the fluid. In the above parameter range, the particles tend to drag lighter fluid from the upper layer into the stratified region, thus increasing the drag on them substantially and decelerating them within the stratified layer. In the Froude number $Fr_1 = U_1/Nd_p$ range investigated, $3 < Fr_1 < 10$, where N is the buoyancy frequency of the stratified layer, the drag coefficient was found to be an order of magnitude larger than its homogeneous-fluid counterpart. The internal-wave contribution to the drag was small compared to that of fluid dragged into the stratified layer, but substantial internal-wave activity could be detected after the fluid dragged from the lighter layer (the caudal fluid) detached from the particle.

The minimum velocity of the solid particle within the stratified layer was found to be given by $U_{min}/U_1 = 5.5 \times 10^{-2} Fr_1^{9/10}$, occurring on a time scale $t_{min}/(d_p^2/\nu) = 1.4 \times 10^2 Re_1^{-1.7}$, where t_{min} was measured relative to the time of the particle's entry into the stratified region. Outside the parameter range $1.5 < Re_1 < 15$, the drag on the sphere in the density-stratified layer could be approximated to that in a homogeneous fluid, whence the bringing of lighter fluid into the stratified layer as a tail behind the descending particle was found to be negligible.

1. Introduction

Settling and dispersion of solid or liquid particles through density-stratified backgrounds are closely linked with many environmental problems, especially the distribution of pollutants in the lower atmosphere and upper ocean. Airborne solid or liquid particles with diameter d_p smaller than 20 μm are called *aerosols* whereas

† Author to whom correspondence should be addressed: e-mail J.Fernando@asu.edu.

solid particles with $d_p > 20$ μm are called *dust*. The solid particles are usually called particulate matter (PM), the concentration of which is used as a measure of the 'air quality' by environmental regulatory agencies. A multitude of atmospheric phenomena such as pollution episodes at local scales, spectacular sunsets that have followed major volcanic eruptions in the past (Kellog 1990), the nuclear winter that may result from nuclear explosions (Turco *et al.* 1993) and to a certain extent the global climatic variability are attributed to these suspended particles. Solid particles (or marine snow) in the upper ocean have an important bearing on the vertical distribution of biomass, rates of primary production, biochemical cycling and the adaptation of phytoplankton cells to ambient light intensities (Lande & Wood 1987).

Dense solid particles in the environment settle with time, and the settling rates are the key to the assessment of environmental impacts of solid particles. Although it is well known that any foreign matter introduced into stable atmospheric (Kellog 1990) and oceanic (MacIntyre, Alldredge & Gotschalk 1995) layers tends to persist there much longer than it would in neutrally stratified layers, to our knowledge no detailed experimental studies exist delving into the mechanisms responsible for such low settling rates. This paper reports a study that deals with the settling of individual solid particles through quiescent stably stratified fluids, which is a precursor to understand particle settling in more complicated cases, for example in the presence of background turbulence and stratification (Huppert, Turner & Hallworth 1995) or a stratified mean flow. We will show that, under certain conditions, particles settling in stable layers are subjected to greatly enhanced drag forces and elucidate a possible mechanism for this observation.

Although reported laboratory studies on rigid-particle settling through density-stratified miscible fluids are virtually non-existent, the literature on the penetration (or 'breakthrough') of particles through liquid–liquid interfaces between two immiscible liquids is voluminous. These studies have documented plausible scenarios associated with such breakthroughs, when the migrating particles are in a different phase than the liquids or when the particles coalesce with the second liquid after their passage through the first one. In the former case, for example, when a solid particle passes from a 'layer 1' to a 'layer 2' through an interface, two modes of evolution are possible (figure 1), i.e. either the 'film draining mode' characterized by the draining of 'layer 1' fluid trapped between the particle and the interface to yield an ever-thinning film or the 'tailing mode' wherein the particle enters into the 'layer 2' beyond the original interface while remaining encapsulated by the original 'layer 1' fluid which is connected with its main body by a thread-like tail. A number of experiments (Hartland 1968; Shah, Wasan & Kintner 1972) and theoretical analyses (Jones & Willson 1978; Smith & Van De Ven 1984) have been reported on the film drainage mode, but the corresponding studies on the tailing mode are sparse (Maru, Wasan & Kintner 1971; Geller, Lee & Leal 1986). No exact criterion is yet available to predict which mode prevails during the particle passage, although the numerical simulations of Geller *et al.* (1986) have identified the parameters governing these processes for immiscible fluids in the low Reynolds number (or the creeping flow) limit. The numerical study of Geller *et al.* (1986) was preceded by the analytical work of Lee, Chadwick & Leal (1979) and Lee & Leal (1982), who obtained approximate solutions for the translation of a solid sphere perpendicular or parallel to an initially flat interface between two immiscible fluids, and the work of Berdan & Leal (1982) who obtained the solution for the case of rotational motion about a single axis of a solid sphere near a plane interface. All of the above studies assumed the creeping flow limit, and hence the inertial effects were unaccounted for. The analytical studies have

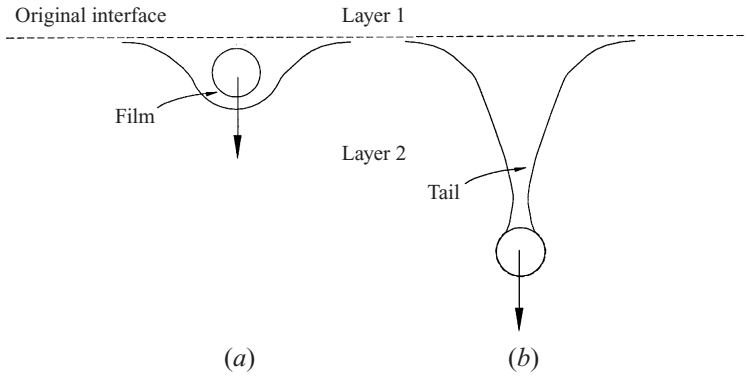

FIGURE 1. Schematic sketches showing (*a*) 'film draining' and (*b*) 'tailing' modes.

been confined to small deformations, and they predicted an increase of the drag force on the particle as the interface is approached. The numerical studies were terminated before the complete breakthrough of the particle from one layer to another, because of computational restrictions. A few studies have been reported on the static instability of a cylindrical-shaped (Princen & Mason 1965) or a spherical-shaped (Maru *et al.* 1971) object resting on an interface between two immiscible fluids.

For the configuration shown in figure 1, for complete breakthrough, the particle and surrounding fluid should be completely disassociated from the top layer. The mechanisms responsible for such a separation, however, are not well understood yet. One possible mechanism is the rupture of the film around the particle and the retreat of the detached film from the particle into the parent 'layer 1'. Another mechanism is the degeneration of the trailing fluid layer due to instabilities of the cylindrical tail (the caudal fluid). Maru *et al.* (1971) have reported observations on varicose instabilities of such tails, which lead to the formation of drops during the breakup of the tail, after a particle penetrates about 120 sphere diameters into the 'layer 2'. During the breakup process, the particles can remain encapsulated by a thin film of 'layer 1' fluid, even after the connection between the particle and the parent fluid layer is severed. Observations of Maru *et al.* (1971) show that the volume of fluid carried by the sphere is directly proportional to the diameter of the sphere and is inversely proportional to the surface tension and the viscosity of 'liquid 1'. The distance from the interface to the breakup point of the caudal fluid column is inversely proportional to the surface tension. During the final stages of this breakup, the liquid film is so small that the usual continuum fluid mechanics approach is not valid, whereupon molecular dynamics may play a leading role (for example, see Kadanoff 1997).

There are several other related studies on the penetration of particles through interfaces. Thornham & Wilson (1983) have considered theoretically, the settling of a porous body through a density interface between two immiscible fluids and illustrated that the interface outside the particle remains undisturbed, but dips down inside the particle. This analysis, however, neglected the hydrodynamic drag and assumed that the weight of the body is in balance with the buoyancy force. Another related aspect is the generation of internal waves as particles move through a density interface. This topic has also received only little attention, although there are numerous studies on the generation of internal waves by bodies moving in unbounded, continuously stratified fluids (Mowbray & Rarity 1967; Lighthill 1996). The energy radiated by these waves can exert an additional drag on the body, as was shown by Warren (1960) in a study dealing with the uniform vertical motion of a body in a linearly

stratified fluid. Finite-amplitude oscillations of spheres at their neutrally buoyant levels have been treated theoretically by Larsen (1969) and the dynamics of a thermal conducting sphere settling through a thermally stratified fluid has been considered by Nikiforovich & Dudchak (1992). Existing literature also abounds with publications on the dynamics of fluid drops or bubbles rising toward deformable liquid–liquid interfaces (e.g. Shopov & Minev 1992).

Another topic related to bodies moving in fluids is the 'drift', which is defined as the deformation of a material surface initially perpendicular to the direction of motion. Studies on drift were initiated by Darwin (1953) who considered the motion of a solid body through an ideal, homogeneous, incompressible fluid, delving into actual trajectories of fluid particles. The results (which are also the basis of Darwin's theorem) state that, under certain conditions, the drift volume enclosed between the initial and final position is equal to the volume corresponding to the hydrodynamic added mass. Although the concept of drift was further extended by Lighthill (1956), immediately following the work of Darwin, it appears to have then been forgotten for many years. The interest on this topic, however, has been resuscitated recently and the conditions for the equality of drifted and added masses have been rigorously delineated Yih 1985; Benjamin 1986; Eames, Belcher & Hunt 1994; Eames, Hunt & Belcher 1996; Eames & Hunt 1997).

As is evident from the foregoing discussion, most of the investigations on the motion of particles near or through interfaces have been theoretical or numerical in nature and have been concerned with the low-Reynolds-number motion of particles through immiscible fluids of different physical properties. These interfaces are only a few molecular diameters thick and the surface tension plays a leading role in their dynamics. This contrasts with the situations found in environmental flows where the fluid layers are miscible (and hence surface tension effects are irrelevant), the stratification changes on scales larger than the particle diameter (fluid can be treated as continuously stratified), physical properties except the density do not vary significantly from layer to layer and the particle Reynolds numbers are small to moderate. To our knowledge, there is no reported experimental or theoretical work on particles settling under such conditions; the work reported herein attempts to fill this gap.

2. Experimental method

The experiments were carried out in a transparent tank of dimensions $30 \times 60 \times 60$ cm. The working fluid was prepared by first introducing a layer of lighter fluid into the tank and then slowly feeding a layer of dense fluid underneath the lighter layer as a sheet via a capped hole. The lighter fluid was a layer of 200 proof ethyl alcohol and water mixture of approximate thickness 25 cm. The bottom layer was a solution of salt water of approximately the same thickness. The concentrations of alcohol and salt were selected so that the refractive indices of the two layers are the same, thus providing an optically uniform, miscible, three-layer fluid with a diffused density interface sandwiched between homogeneous fluid layers. The refractive–index matching was required to eliminate errors associated with the wandering of light beams due to refractive index changes, when using optical imaging techniques. Since aqueous alcohol and salt solutions are fully miscible in all proportions, the density interface between the layers was thick due to local mixing at the interface, of the order of 2–4 cm, and the fluid within it had a continuous density distribution. The ratio of densities of the lower (ρ_2) to upper layer (ρ_1) was varied in the range 1.025 to 1.065. Typical dynamic

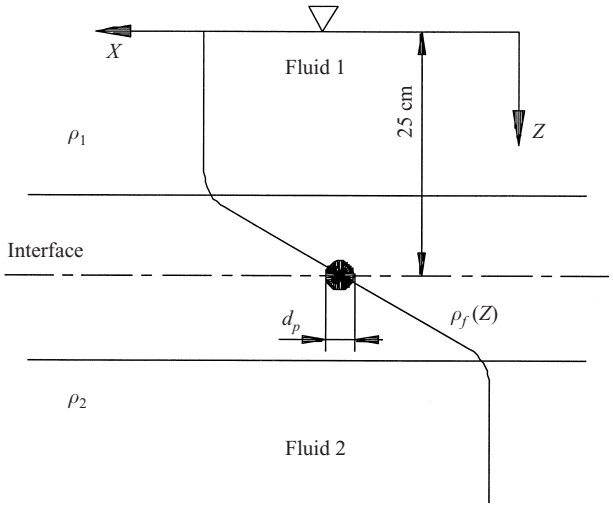

FIGURE 2. Schematic sketch showing the problem considered.

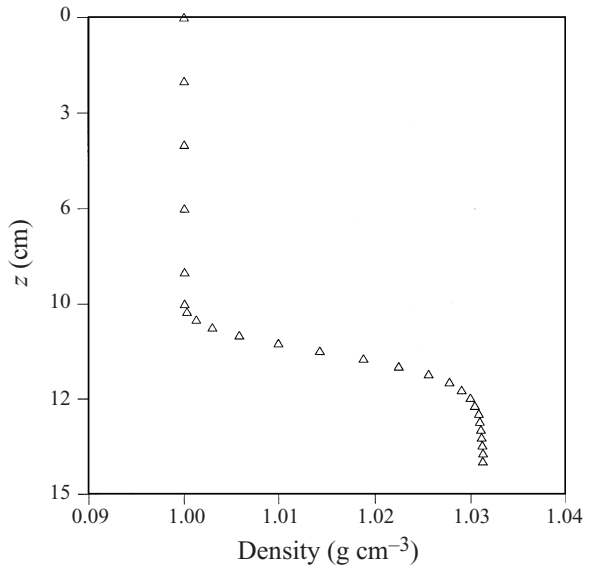

FIGURE 3. A typical vertical density profile taken at the beginning of an experiment with $\rho_2/\rho_1 = 1.031$.

viscosities of the upper and lower layers were 1.17×10^{-3} and 1.19×10^{-3} kg m^{-1}s^{-1}, respectively, and hence the viscosity changes across the layers could be neglected. The density measurements were taken by traversing a conductivity probe, properly calibrated to account for the conductivity variation in alcohol–salt mixtures (Perera, Fernando & Boyer 1994). A schematic of the flow configuration used in the present study is shown in figure 2, and a typical measured density profile is shown in figure 3.

Spherical polystyrene particles in the density range 1.025 to 1.049 g cm^{-3} and in the diameter range 0.25 to 1.80 mm were used for the experiments. These particles were soaked in a wetting agent, and individual particles were released from just below the upper fluid surface at the centre of the tank cross-section. The size of each particle

was measured using a micrometer before the experiments. Visualization of descending particles was performed by illumination of the vertical centreplane, along the long axis of the tank, using a 0.5 cm thick sheet of light. The descents of the particles were video recorded from a direction normal to the light sheet.

A particle tracking system was used to obtain velocity measurements. The system is based on a PC 486DX computer, equipped with a Data Translation DT-2861 video frame grabber. A standard monochrome CCD video camera was used, and the video signal was recorded using an NTSC S-VHS video recorder. Video recordings were processed using the DigImage software package. Details of this particle tracking system can be found in Dalziel (1992, 1993) and Drayton (1993).

The particle position is defined as the centroid of light intensity, and hence the particle image has to extend at least two pixels in each direction in order to obtain the particle position with subpixel accuracy. The size of the particle image depends on the physical size of the particle, its reflective properties and the optical arrangement. In order to satisfy the above criterion, the vertical size of the field of view had to be adjusted in each experiment such that the image of the smallest particle used is larger than 2×2 pixels.

The time step used for tracking varied within the range 0.066 to 0.2 s. The magnitude of the time step was chosen according to the magnitude of the particle settling velocity. Velocity was calculated using a least-squares line fitted through five neighbouring points of the trajectory.

Typical error in the slope of the least-squares line is given by Dalziel (1992):

$$\Delta_{v_i} = \left[\frac{12}{m(m+1)(m+2)}\right]^{1/2} \frac{\Delta_{x_i}}{\Delta t} \frac{h}{480} \quad \text{cm s}^{-1}, \tag{2.1}$$

where m is the number of time separations used for fitting the quadratic function, Δt the time step used for tracking, Δ_{x_i} the accuracy in determining the position of particles expressed in pixels and h the vertical size of the field of view in cm. For the particular setup of experiments with $m = 4$, $\Delta_{x_i} = 0.2$ pixels, $\Delta t = 0.066$–0.2 s and $h = 12$–20 cm, it was found that $\Delta_{v_i} \leqslant 0.026$ cm s^{-1}.

In order to gain a better insight into phenomena occurring during the passage of a sphere through the interface, a set of experiments was carried out with the aim of following particles within the interfacial region at a higher magnification. To this end, a small amount of dye (sodium fluorescein) was injected at the level where the density begins to increase at the base of the top layer. The plane of descent was illuminated by a sheet of argon–ion laser light, and a precision video microscope (Infinity/VAR) was used to magnify the region of interest. Typical magnifications used and the vertical dimension of the field of view of the microscope were in the range 10–20 and 10–25 mm, respectively.

In these experiments, too, careful matching of refractive indices was critical, as the usage of video microscopes in optically inhomogeneous media creates serious problems due to large image distortions. The position of the particle was found in each image and the particle size itself was used as the scale for establishing the connection between the pixel coordinate system and the laboratory coordinate system. The usual way of establishing the connection between pixel and laboratory coordinate systems by using a grid-engraved Perspex sheet was untenable for this case; small errors in grid positioning can result in large errors in particle position, because of the large magnification of the video microscope. Fortunately, the particle boundaries were well resolved by the video microscope, thus providing calibration points.

In addition to velocity measurements, the volume of the upper-layer fluid dragged into the interfacial region was also measured by using images obtained by the video microscope. Light intensity contours, corresponding to the boundary between the fluid dragged from the upper layer and the surrounding fluid, were measured for each tracked position of the particle within the stratified region. The above measurements, together with the vertical density distribution measured before the experiment by a traversing conductivity probe, and the assumptions (*a*) the tail behind the particle is axisymmetric, and (*b*) the density profile in the outer stratified region remains undisturbed, were used to calculate the buoyancy force acting on the fluid column dragged from the upper layer behind the particle.

3. Experimental results

3.1. *Observations on the settling of particles*

The simplest possible scenario for the settling of a particle in a stratified fluid is that the descent occurs in a series of infinitesimally small steps, wherein the particle responds rapidly to background conditions so that the particle velocity is the same as the local terminal velocity. Observations, however, show that the behaviour of particles can be markedly different from the above scenario. Figure 4 shows plots of the dimensional velocity versus the distance travelled from the top of the viewing region (which is located 13.5 cm from the top of the upper layer) for several particle diameters d_p and interfacial buoyancy jumps Δb.

Note that the particle velocities U are approximately constant in the bulk of the upper layer and then they show a significant decrease as particles descend through the interface. A noteworthy observation is the existence of a velocity minimum U_{min} in the stratified layer which is often located in the lower part of the stratified layer. For the cases shown, Δb was 25, 31 and 64 cm s^{-2}, and the percentage reductions of the speed $(U_2 - U_{min})/U_2$ were 12.5%, 20% and 50%, respectively, indicating that the velocity reduction is more pronounced at larger density jumps; however, at larger density jumps, the persistence time of these low velocities ($< U_2$) is smaller.

Figure 5 shows the same information as figure 4, but obtained from experiments where the video microscope was used for (high resolution) measurements together with the density profile. Here the velocity is resolved with a time step of 0.066 s and hence the decrease of velocity is evaluated with a higher accuracy. Because of the limited field of view, the data could be acquired only within a portion of the stratified layer. The data are plotted in terms of the normalized velocity, where the normalization was performed using the local terminal velocity U_t calculated using the standard equations (White 1991)

$$(\rho_p - \rho_f)V_p g = C_D \tfrac{1}{2}\rho_f U_t^2 S_p, \tag{3.1}$$

$$C_D = \frac{24}{Re_t} + \frac{6}{(1 + Re_t^{1/2})} + 0.4. \tag{3.2}$$

Here ρ_f is the density of ambient fluid at a given position of the particle, ρ_p is the density of the particle, $V_p = d_p^3\pi/6$ and $S_p = d_p^2\pi/4$ are the volume and cross-sectional area of the particle, respectively, C_D is the drag coefficient based on the local Reynolds number $Re_t = d_p U_t/\nu$ and ν is the local kinematic viscosity of the fluid. Note that (3.2) is based on previous drag data obtained from particle motion studies in non-stratified fluids (White 1991).

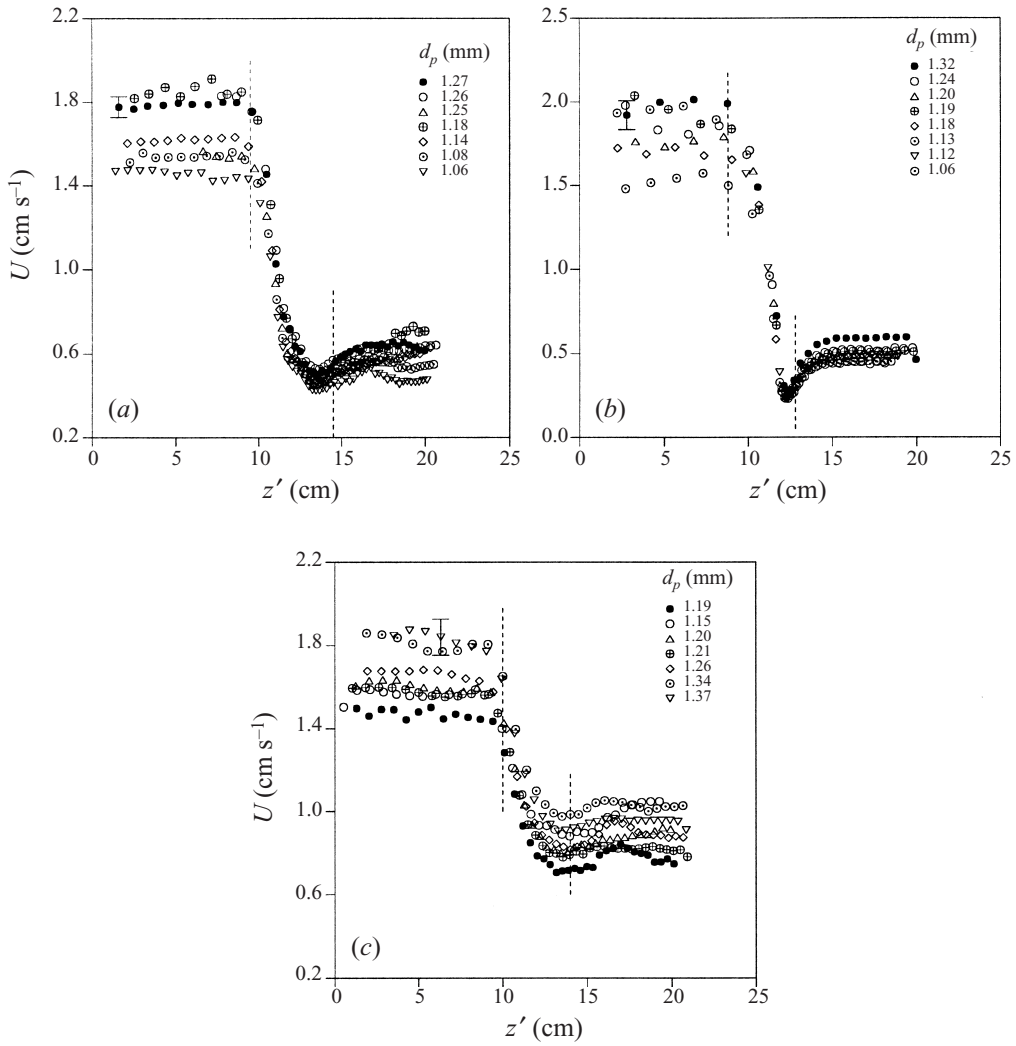

FIGURE 4. The dimensional velocity of a particle versus the distance travelled from the top of the viewing region z': (*a*) the buoyancy jump $\Delta b = 31$ cm s^{-2}; (*b*) $\Delta b = 64$ cm s^{-2}; (*c*) $\Delta b = 25$ cm s^{-2}. The vertical dashed lines indicate the edges of the stratified region.

As evident from figures 4 and 5, within the stratified layer the particle velocity first reduces and then increases gradually. Within the interface, the minimum velocity of a particle can be as low as 10% of the local terminal velocity. As mentioned, the distances shown are limited to the vertical field of view of the microscope, but a composite diagram of particle velocity/distance data obtained with and without the video microscope shows that the particles achieve their terminal velocities corresponding to the upper and lower layers, respectively, before entering the interface and after travelling several tens of particle diameters beyond the interface.

Figure 6 shows an image of the magnified view of a particle entering the stratified layer, after travelling with the terminal velocity in the upper homogeneous layer. A major cause of the deceleration of the particle in the stratified layer is apparent here; that is, the dragging of fluid from the upper layer into the stable layer. The buoyancy

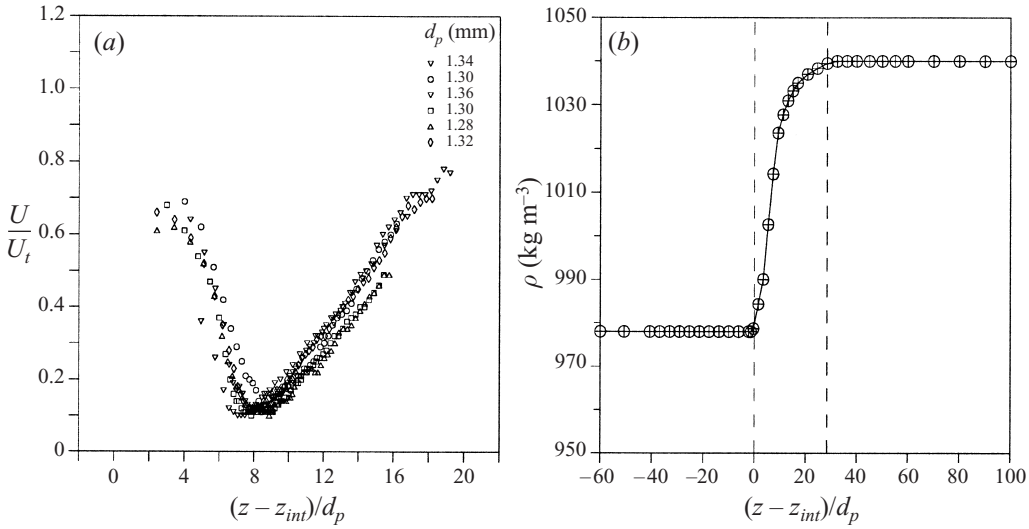

FIGURE 5. (*a*) Normalized particle descent velocity as a function of the distance measured from the top of the interfacial layer (z_{int}). A video microscope was used for the measurements. The local terminal velocity was used for normalization. (*b*) The density profile used for the experiment. The vertical dashed lines indicate the edges of the stratified region.

forces on the caudal fluid impose an additional upward force on the particle, thus causing it to decelerate significantly. Careful inspection of the fluid layer surrounding the sphere indicates that, during the initial penetration, the fluid between the particle and the interface is squeezed off so rapidly that no fluid of the upper layer can be detected around the particle within the resolution of the measurement instrument (i.e., the film drainage mode is untenable).

As the particle descends, the tail is elongated and after some time it separates from the sphere. Drag measurements to be discussed later and the velocity measurements depicted in figures 4 and 5 show that, after separating from the caudal fluid, the particle gradually approaches its local terminal velocity (calculated on the basis of (3.2)). This observation indicates that the caudal fluid is completely disassociated from the particle and that no fluid belonging to the upper layer encapsulates the particle. Thus, it is likely that the separation of caudal fluid occurs by the rupture of fluid film around the particle and not by the instabilities of the tail as discussed in §1. In the latter case, it is possible to expect a light fluid film to encapsulate the particle after the breakup of the tail.

A sequence of images acquired from the video tape, 0.1 s apart, as a particle breaks through an interface, is shown on figure 7. Note that only the upper portion of the interface is dyed and the entire depth shown below the dyed region of each frame is within the interface. Morphological filtering of images (which enhance the boundaries of features) was applied in order to emphasize the overall structure of the images. Although some of the details in the vicinity of the particle are smeared by this operation, the events taking place during the breakthrough are quite clear. Frames 1–5 show the initial penetration and the development of a tail behind the particle. Frame 5 shows the configuration just before the tail separation and frame 6 was taken soon after the separation. Note the retraction of the lower-density fluid to its original position and simultaneous generation of internal waves in the stratified layer (frames 6–12) after the fluid layers retract to their equilibrium positions. The

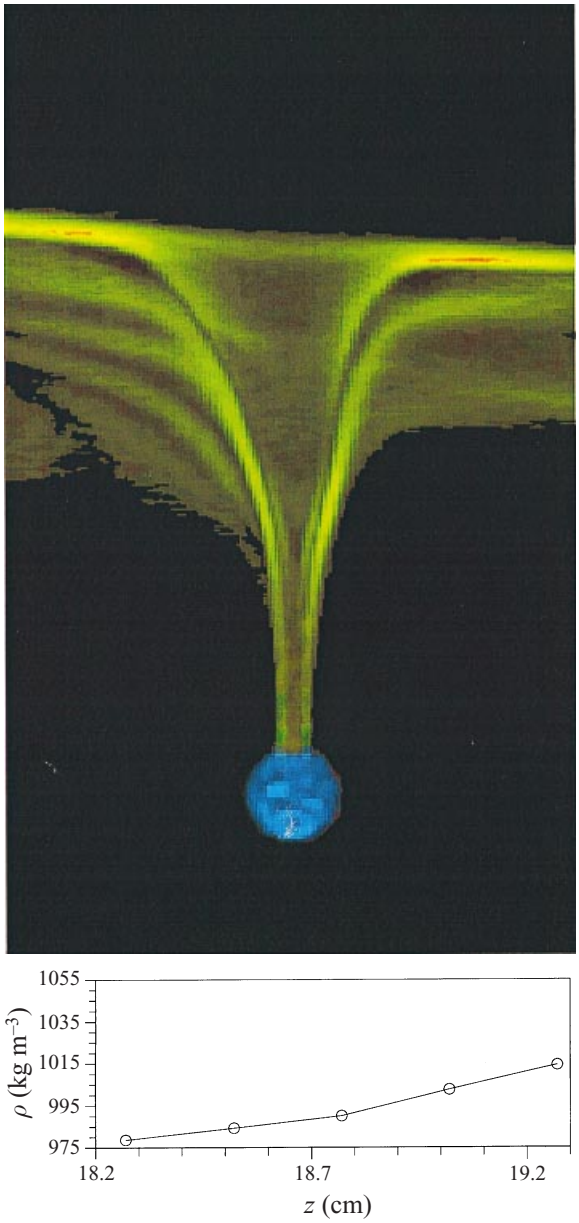

FIGURE 6. A particle passing through the interface and the density profile within the field of view. No morphological filtering was applied in this figure. $d_p = 1.3$ mm.

drag observations to be discussed later indicate that, when the tail is still attached to the particle, the contribution of internal waves to the total drag on the sphere is relatively small compared to that induced by the upward buoyancy force on the tail. This observation is in agreement with the observations of figure 7 which show that the internal waves are mainly generated after the sphere has been separated from the tail, during the rebounding of the lighter fluid elements to their original levels; the waves observed are a result of the release of potential energy during the rebounding of lighter fluid.

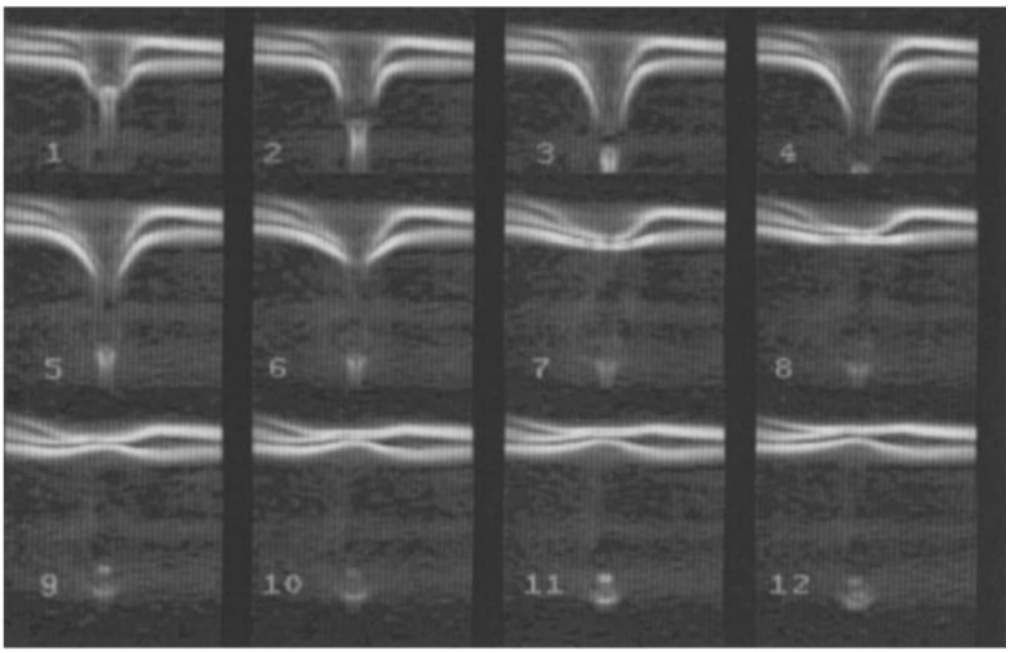

FIGURE 7. A video-microscopic sequence of a particle passing through the interface. $d_p = 1.3$ mm.

3.2. *Drag measurements in homogeneous fluids*

For the purpose of checking the data handling and reduction procedure, a number of experiments were performed with spherical particles settling in homogeneous fluids. The methodology used was to calculate the drag coefficient of the particle by evaluating individual terms of the equation of motion of the particle. The equation of motion in the vertical direction, for a particle released from the rest in a quiescent fluid, can be written in the form

$$\rho_p V_p \frac{\mathrm{d}U}{\mathrm{d}t} = (\rho_p - \rho_f) V_p g - C_D^H \tfrac{1}{2} \rho_f U^2 S_p + (F_A + F_H), \tag{3.3}$$

where U is the particle velocity at time t. The term on the left-hand side is the inertia force acting upon the particle, arising due to an imbalance of forces. The first term on the right-hand side is the buoyancy force acting on the particle. The second term represents the 'steady-state' drag corresponding to the instant being considered. Two additional terms, the inertia force of added mass F_A and the history term (Basset force) F_H are due to the unsteadiness of the particle motion. The drag coefficient C_D^H includes the form and skin friction drag terms, and it depends on the Reynolds number according to (3.2). In the limit of potential flow and zero background flow, F_A can be written as

$$F_A = -\frac{\rho_f}{2} V_p \frac{\mathrm{d}U}{\mathrm{d}t}. \tag{3.4a}$$

In the creeping flow limit the analytic solution for F_H can be written as

$$F_H = -\frac{3d_p^2}{2} (\pi \rho_f \mu)^{\frac{1}{2}} \int_{-\infty}^{t} \dot{U}(s) \frac{\mathrm{d}s}{(t-s)^{\frac{1}{2}}}. \tag{3.4b}$$

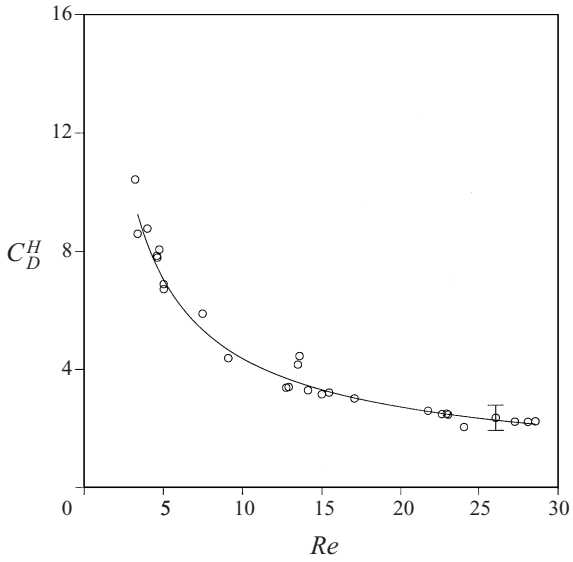

FIGURE 8. The total drag coefficient C_D^H (calculated using (3.3) and velocity measurements) in a homogeneous fluid vs. Reynolds number: ○, present data; ———, recommended drag correlation curve by White (1991).

The efficacy of the forms F_A and F_H given above for the accelerating motion of a sphere beyond the creeping flow range has been considered experimentally by Odar & Hamilton (1963). The parameter range $0 < Re < 62$, where $Re = d_p U/\nu$ is the instantaneous Reynolds number, was used in the experiments. Their results suggested the necessity of modifying (3.4*a*) and (3.4*b*) by introducing empirical coefficients C_A and C_H to correct for the influence of viscous effects and finite fluid inertia, respectively; they proposed:

$$F_A + F_H = -C_A \frac{\rho_f}{2} V_p \frac{\mathrm{d}U}{\mathrm{d}t} - C_H \frac{3d_p^2}{2}(\pi\rho_f\mu)^{1/2} \int_{-\infty}^{t} \dot{U}(s) \frac{\mathrm{d}s}{(t-s)^{1/2}}. \tag{3.5}$$

Both coefficients, C_A and C_H, were obtained experimentally by considering the harmonic motion of a sphere in an otherwise still fluid. They found that C_A and C_H were dependent only on the acceleration modulus, $M_A = (\mathrm{d}U/\mathrm{d}t)/(U^2/d)$, according to the following relations (also see Clift, Grace & Weber 1978):

$$C_A = 2.1 - 0.132M_A^2/(1 + 0.12M_A^2) \tag{3.6a}$$

and

$$C_H = 0.48 + 0.52M_A^3/(1 + M_A)^3. \tag{3.6b}$$

Recent studies (see Magnaudet 1997) have shown that the kernel in the expression for the history terms in (3.4*b*) and (3.5) is correct only at short times, and the partition between the added mass effect and the history term advocated by Odar & Hamilton (1963) may not be accurate. However, the expression (3.5) was found to be a good representation for the cumulative effects of history and virtual mass terms. Since our study is concerned with the additive effect of these two forces, (3.5) and (3.6*a*,*b*) can still be used to estimate the combined magnitude of F_A and F_H.

Figure 8 shows the drag coefficient, evaluated using the measurements of $U(t)$ and the expressions (3.3), (3.5) and (3.6*a*,*b*), as a function of the instantaneous Reynolds

number Re. The data include the measurements taken during the initial adjustment of the particle from zero velocity to the terminal speed and those taken during steady settling. In the former case, all of the terms in (3.3) are expected to make a contribution whereas the latter case is determined by the second and third terms only ($\dot{U}(t) = 0$). Note that in the Reynolds number range investigated, $3 < Re < 28$, the drag coefficient C_D is a strong function of Re. The solid line is the empirical drag coefficient function proposed by White (1991) given by (3.2), based on measurements taken during steady motion of spheres. Note that there is an excellent agreement between (3.2) and the present data, indicating the validity of the methodology used here to calculate C_D^H. The C_D^H values measured at a given *in situ* Reynolds number during unsteady motion of particles are very close to those measured under steady translation of spheres at the same Re given by (3.2). This suggests that, in the Re range covered by the experiments, the motion of particles can be considered as occurring in a series of quasi-steady steps. Calculations also show that, during the unsteady motion, all of the terms in (3.3) play a role, except the last (Basset) term which appears to be small compared to other terms. Finally, it should be noted that the macroscopic equations (3.3), (3.5) and (3.6*a,b*) used in the drag calculation are only approximate semi-empirical expressions; lacking an exact Navier–Stokes-equation-based solution for the flow field around the particle at moderate Reynolds numbers, (3.3)–(3.6*b*) are indeed useful approximate equations. The Re values used in the present study are in between the limiting cases that allow the creeping flow assumption (lower limit) and where the boundary layer approximation is valid (upper limit).

3.3. *Descent of particles in density-stratified fluids*

3.3.1. *Behaviour at different parameter ranges and drag calculations*

In § 3.1, a detailed description of how a particle can be directly affected by the interfacial stratification was presented, wherein the particle drags a column of fluid from the upper layer into the interfacial region. The fluid column elongates as the particle descends, but after a certain distance of travel the tail is broken off and the particle disassociates from the top layer. Extensive observations show that this behaviour occurs in a certain range of entry Reynolds numbers $Re_1 = U_1 d_p/\nu$, more quantitatively in the approximate range $1.5 < Re_1 < 15$; here U_1 is the entry velocity of the particle into the interface, which is the same as the terminal velocity in the upper layer. At larger Re_1, the particle penetrates through the interface dragging only an insignificant amount of upper-layer fluid into the interface because of the flow separation behind the particle. At low Re_1, the dragging of fluid from the top layer does not occur because of the slow descent of particles that allows them to adjust to background conditions. Thus, in the two limits $Re_1 < 1.5$ and $Re_1 > 15$, the drag measurements during the motion of particles within the interface based on (3.3) show a satisfactory agreement with corresponding measurements in homogeneous fluids, indicating insignificant influence of stratification.

Figure 9 shows a set of space–time trajectories of several particle types, having different diameters d_p and densities ρ_p, settling through the same density interface. For clarity, the Reynolds numbers Re_1 for only a few runs are shown. Note the trajectory at the extreme left, corresponding to glass beads ($\rho_p = 2.5$ g cm^{-3}; $d_p = 0.38$ mm); here the particle passes through the interface without significant departure from its behaviour prior to arriving at the interface. The drag coefficient measurements show that it approximately corresponds to the homogeneous case with the same Re_1, thus confirming the independence of drag from major stratification effects. The trajectory at the extreme right corresponds to the low Reynolds number case of $Re_1 = 0.7$

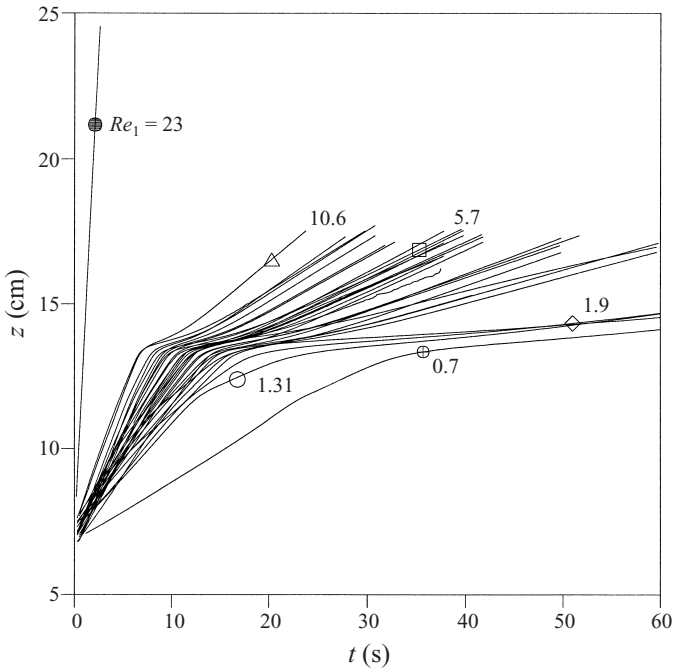

FIGURE 9. The time trajectories of particles. The symbols ● and ⊕ have been used to indicate the largest and smallest Re_1 used: ●, $Re_1 = 23$; ⊕, $Re_1 = 0$. In all experiments, the same density stratification was used with $\Delta b = 38$ cm s^{-2} and the density interface is located at $z = 13$ cm.

carried out with small polystyrene particles ($\rho_p = 1.049$ g cm^{-3}; $d_p = 0.37$ mm). In this case, the particle adjusts to the background as it descends, and the drag changes continuously to satisfy (3.3).

Flow visualization studies show that, when $1.5 < Re_1 < 15$, the dragging of the upper fluid (tailing mode) into the stratified layer is a common feature. As evident from figure 9, the particle trajectories respond to this effect by showing a noticeable decrease of velocity within the interface, until the caudal fluid breaks off from the particle. Although only a limited number of Re_1 runs are shown in figure 9, a large number of experiments with detailed flow visualization were used to detect the possible existence of the 'tailing' mode at different Re_1 and to calculate the drag coefficient. Examining a continuous range of Re_1, however, was not practical and hence the Re_1 range quoted for the appearance of the tailing mode has an error margin of $\pm 15\%$. The possibility of the dependence of this parameter range on other factors will be discussed later.

The drag calculation was performed by modifying (3.3) to include the 'stratification drag', which includes the drag due to caudal fluid and internal waves, namely

$$\rho_p V_p \frac{\mathrm{d}U}{\mathrm{d}t} = (\rho_p - \rho_f) V_p g - (C_D^H + C_S) \tfrac{1}{2} \rho_f U^2 S_p + (F_A + F_H), \tag{3.7}$$

where $C_S = F_S / \frac{1}{2} \rho_f U^2 S_p$ is the drag coefficient introduced to account for the density stratification and F_S is the stratification drag force. Note that F_S and C_S are dependent on a number of variables, ρ_1, U_1, d_p, N, ν and the penetration distance z_1 of particle into the interface:

$$F_S = f_1(\rho_1, U_1, d_p, N, \nu, z_1), \tag{3.8}$$

where $f_1, f_2, \ldots$ are functions. Similar expressions can be written for the instantaneous background density ρ_f of the particle in the stratified layer and velocity U of the particle at a penetration distance z_1; these expressions can be combined with (3.8) to form expressions such as

$$C_S = \frac{F_S}{\frac{1}{2}\rho_f U^2 S_p} = f_2\left(Re_1, Fr_1, \frac{z_1}{d_p}\right), \tag{3.9}$$

and

$$\frac{U}{U_1} = f_3\left(Re_1, Fr_1, \frac{z_1}{d_p}\right), \tag{3.10}$$

where $Re_1 = U_1 d_p/\nu$ and $Fr_1 = U_1/Nd_p$, respectively, are the Reynolds and Froude numbers based on the approach velocity. Similarly, it can be argued that the maximum value of C_S and the minimum value of U should be dependent on Re_1 and Fr_1 only.

Using the distance–time trajectories obtained in the experiments, the terms in (3.7) could be calculated and thus C_S could be evaluated. Figure 10(*a,b*) shows the calculated drag coefficient $C_D^* = (C_D^H + C_S)$ and the dimensional stratification drag F_S as a function of the dimensionless distance penetrated by the particles into the interface $(z - z_{int})/d_p = z_1/d_p$; here z_{int} is the location of the upper surface of the interface. Also shown in figure 10(*c*) is the simultaneous decrease of particle velocity, indicating the occurrence of minimum velocity in concurrence with the maximum drag coefficient. The dependence of drag coefficient C_D^* on governing parameters is discussed below.

Based on the above discussion, the problem of entry of a steadily descending particle into a stratified layer ought to be governed by Re_1 and Fr_1, and thus there is possibility that the Re_1 range where the tailing mode occurs is dependent on Fr_1. Because of the interdependence of Fr_1 and Re_1 through d_p and due to the limited ranges of d_p and N that could be used, only a narrow range of Fr_1 was achievable in the present study. To investigate the influence of Fr_1, sets of experiments were carried out by carefully fixing Fr_1 and by varying Re_1. The occurrence of the tailing mode was diagnosed by evaluating the ratio $(C_D^*)_{max}/C_D^H$, where $(C_D^*)_{max}$ is the maximum drag coefficient on the particle measured during its descent in the stratified layer and C_D^H is the drag coefficient measured in a homogeneous layer corresponding to the *in situ* Reynolds number Re at which $(C_D^*)_{max}$ occurs (i.e. based on (3.2)). The results are shown in figure 11. It is evident that the Re_1 range identified above for the tailing mode, $1.5 < Re < 15$, does not significantly depend on Fr_1, although the magnitude of $(C_D^*)_{max}/C_D^H$ may depend on Fr_1. The solid and dashed lines shown correspond to the best data fit for $Fr_1 = 5$ and $Fr_1 = 3$, respectively. Also note that because of practical limitations, the experiments with the largest Fr_1 ($Fr_1 = 10$) could not be extended to smaller Re_1.

3.3.2. *Minimum velocity within the density interface*

As stated before, a solid particle arriving at the interface with $1.5 < Re_1 < 15$ decelerates within the interface, followed by a velocity minimum U_{min}. Thereafter the particle accelerates to a steady velocity, corresponding to the terminal velocity of the lower layer. Based on the governing parameters discussed in § 3.3.1, it is possible to write U_{min} in the following non-dimensional form:

$$\frac{U_{min}}{(N\nu)^{1/2}} = g\left(\frac{U_1 d_p}{\nu}, \frac{U_1}{Nd_p}\right) = g(Re_1, Fr_1), \tag{3.11}$$

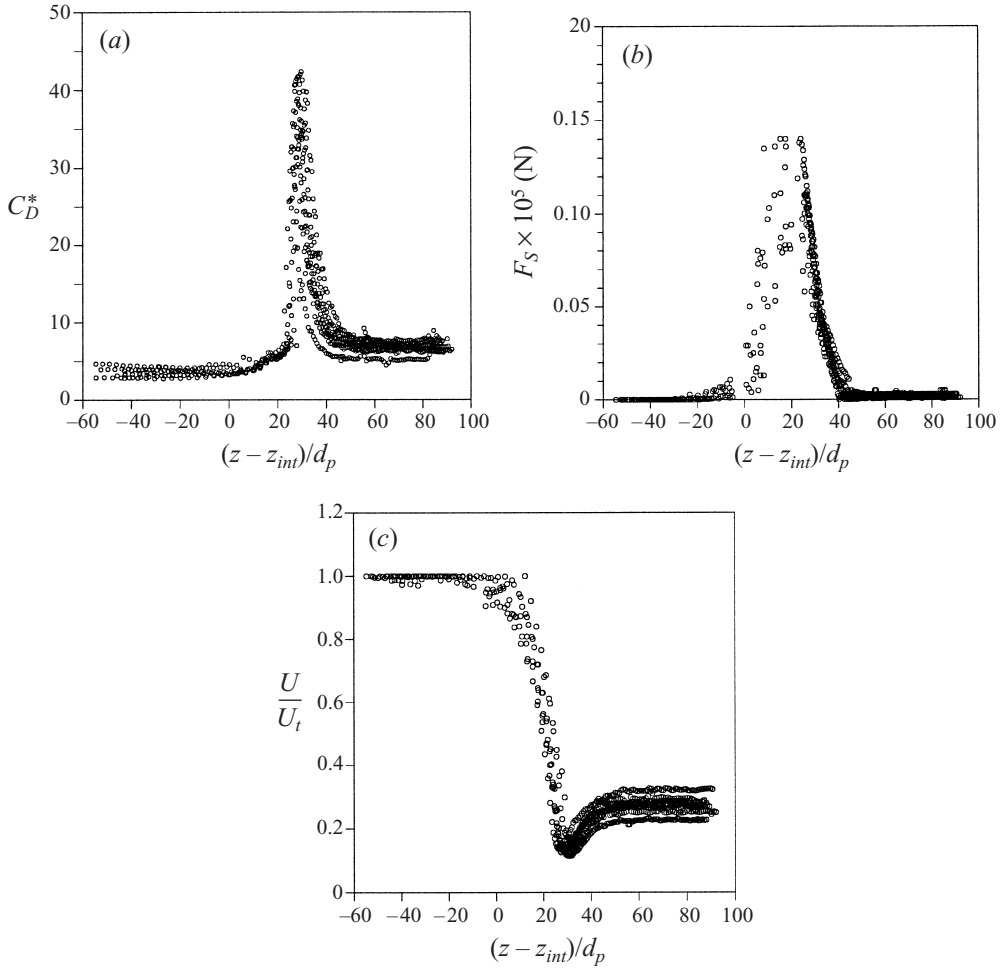

FIGURE 10. (*a*) The variation of the total drag coefficient and (*b*) the drag force (in N) as a function of the dimensionless distance travelled below the interface. The latter is included to depict the increase of drag force. The increase of C_D^* contains the contributions of the stratification drag and the velocity reduction, and hence the change of drag force is not clearly revealed. Note the increase of drag as more and more fluid from the upper layer is dragged into the interface and the decrease of drag as the particle separates from the caudal fluid. A single stratification is shown with $d_p = 1.03$–1.32 mm, $\Delta b = 64$ cm s^{-2}, $\rho_p = 1.048$ g cm^{-3}. (*c*) The velocity of the particle, normalized by the terminal velocity in the upper layer U_1 as a function of the dimensionless travel distance below the interface.

where g is a function. Figure 12 shows a plot of $U_{min}/(Nv)^{1/2}$ as a function of Re_1 for $Fr_1 = 3$, 5 and 10; it is clear that the non-dimensional minimum velocity is a function of both Re_1 and Fr_1. The data tend to group into three clusters, depending on Fr_1. An attempt was made to collapse the data of figure 12 by using an expression of the form

$$\frac{U_{min}}{(Nv)^{1/2}} = \alpha Re_1^n Fr_1^m, \tag{3.12}$$

and the best collapse (based on least-square fits and minimum error criterion) of data was found to occur when $m = 7/5$ and $n = 1/2$. Figure 13 shows a plot of

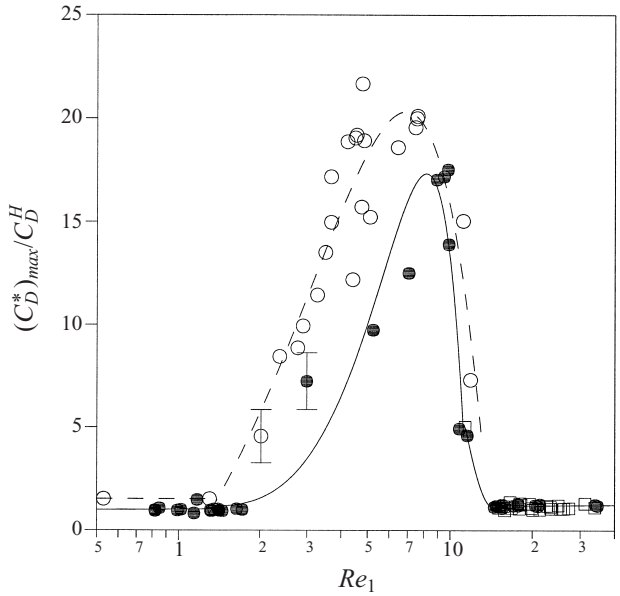

FIGURE 11. $(C_D^*)_{max}/C_D^H$ as a function of Re_1, for different Fr_1 indicated. Here $(C_D^*)_{max}$ is the maximum drag coefficient measured in the stratified layer, say, corresponding to the instantaneous Reynolds number Re_c and C_D^H is the drag coefficient in a homogeneous fluid at Re_c. ○, $Fr_1 = 3$; ●, $Fr_1 = 5$; □, $Fr_1 = 10$.

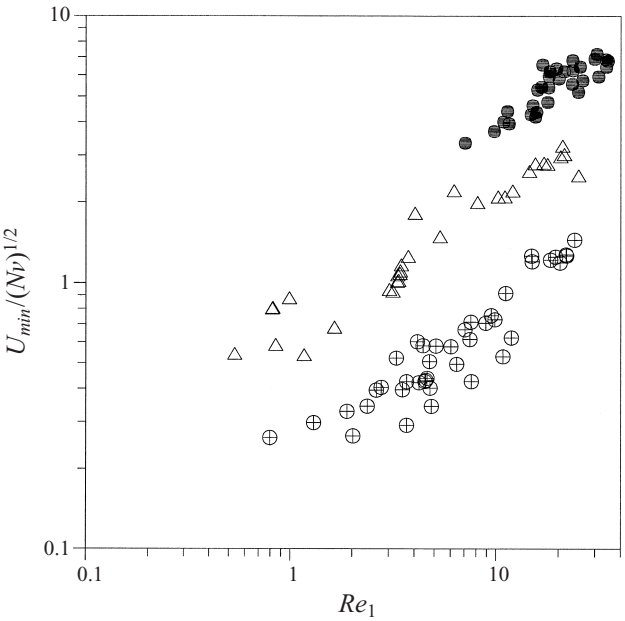

FIGURE 12. The non-dimensional velocity minimum as a function of the Reynolds and Froude numbers: ●, $Fr_1 = 10$; △, $Fr_1 = 5$; ⊕, $Fr_1 = 3$.

$U_{min}/(Nv)^{1/2}$ versus $Fr_1^{7/5}Re_1^{1/2}$; the data indicate an expression of the form

$$\frac{U_{min}}{(Nv)^{1/2}} = 5.5 \times 10^{-2} Re_1^{1/2} Fr_1^{7/5}. \tag{3.13}$$

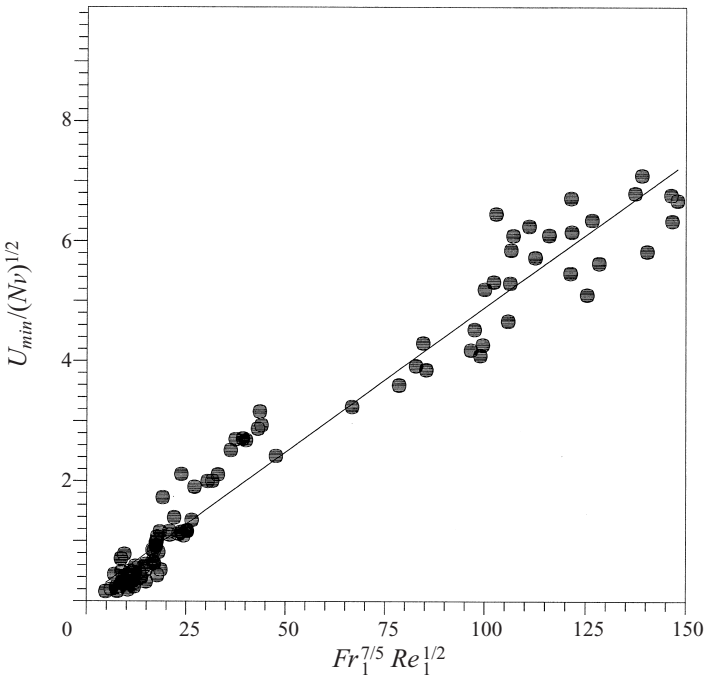

FIGURE 13. A plot of the normalized minimum velocity $U_{min}/(Nv)^{1/2}$ versus $Fr_1^{7/5}Re_1^{1/2}$.

It is interesting that, according to (3.13), U_{min} is independent of viscosity, and takes the form $U_{min}/U_1 \sim Fr_1^{9/10}$, indicating U_1 is a better scale for U_{min} than $(Nv)^{1/2}$.

Likewise, the time taken by the particle in the stratified layer to achieve the minimum velocity should also be dependent on Fr_1 and Re_1, according to

$$t_{min}/(d_p^2/v) = g_1(Re_1, Fr_1), \tag{3.14}$$

where g_1 is a function. Figure 14 shows a plot of non-dimensional t_{min}, plotted as a function of Re_1 for different Fr_1. In the Fr_1 range considered, $t_{min}/(d_p^2/v)$ is a function of Re_1, independent of Fr_1. The best fit data in the range $1.5 < Re_1 < 15$ gives $t_{min}/(d_p^2/v) = 1.4 \times 10^2 Re_1^{-1.7}$.

3.3.3. *Contributions to the stratification drag*

The stratification drag is contributed to by several effects, such as the dragging of caudal fluid from above, internal waves and 'modification' of flow structure around the particle due to the density gradient. In an attempt to separate drag forces due to the caudal fluid from the other effects described above, the buoyancy force on the particle due to caudal fluid was calculated using video-microscopic images as follows. The outer edge of the dragged layer was located in images as described in § 2, and the fluid volume contained within it (see schematic of figure 15) was calculated using the assumption of an axisymmetric tailing fluid column. The buoyancy force associated with the fluid column (or the drag force on the particle due to caudal fluid) could be evaluated as

$$F_{SD} = \pi g \int_0^{z_p} x^2[\rho(z_1) - \rho(0)]\mathrm{d}z_1, \tag{3.15}$$

where the upper limit z_p is defined by the location of the solid particle, z_1 is the distance measured downward from the top of the interface, x is the radius of the

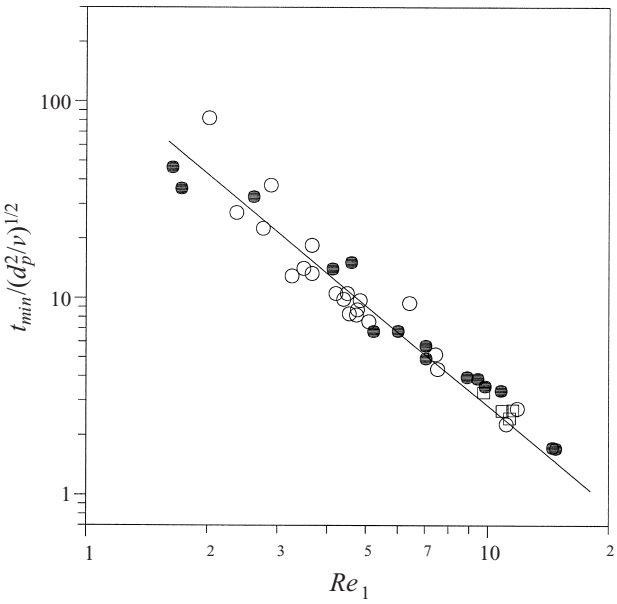

FIGURE 14. The dependence of normalized time to achieve the minimum velocity as a function of the entry Reynolds number Re_1. Runs corresponding to different entry Froude numbers Fr_1 are shown. ○, $Fr_1 = 3$; ●, $Fr_1 = 5$; □, $Fr_1 = 10$.

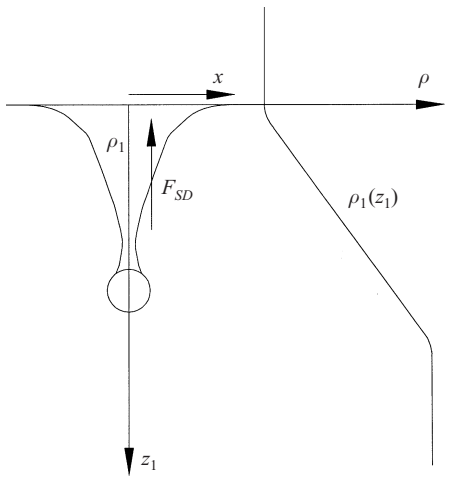

FIGURE 15. Schematic sketch of the drifted fluid volume, forces acting on it, and the density profile of the ambient fluid.

caudal fluid column at z_1 and $\rho(0) = \rho_1$. The stratification drag coefficient due to the caudal fluid alone can be defined as $C_{SD} = F_{SD}/\frac{1}{2}\rho_f S_p U^2$, which together with the drag coefficient due to other stratification effects C_{ID} contribute to the total stratification drag coefficient $C_S = C_{SD} + C_{ID}$.

In the spirit of the observation discussed in §3.3.1 that, when the stratification drag is absent, the total measured drag coefficient C_D^* of particles settling in stratified layers approaches that of a homogeneous fluid C_D^H at the same Re, the stratification drag coefficient could be estimated by $C_S = C_D^* - C_D^H$. The drag coefficient ratio C_S/C_D^H calculated directly using the method discussed in §3.3.1 (i.e. based on the equation of

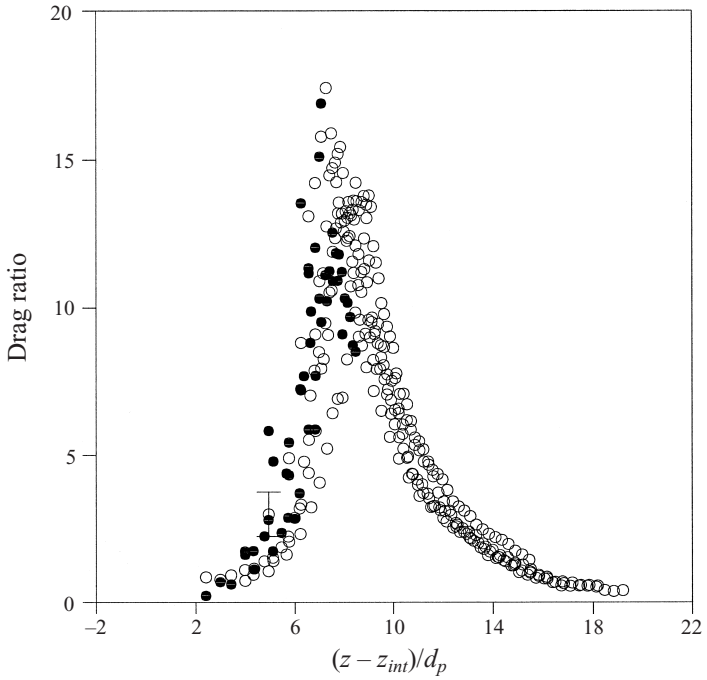

FIGURE 16. The ratios of drag coefficients C_S/C_D^H versus the normalized distance travelled by the particle, as measured from the top edge of the density interface for several runs, at $Re_1 \approx 10$ and $Fr_1 \approx 3$: ●, drag ratio with C_S calculated on the basis of the buoyancy force acting on the drifted fluid; ○, C_S calculated on the basis of $C_D^* - C_D^H$.

motion (3.7)) for several experiments with $Re_1 \approx 10$ and $Fr_1 \approx 3$ is shown in figure 16 by the open symbols. The ratio C_{SD}/C_D^H directly measured using (3.15) (i.e. based on the caudal fluid volume) is shown on the same figure by the solid symbols. Here the horizontal axis is selected to indicate the position of the particle relative to the upper surface of the interface. As the particle descends, the caudal fluid column elongates until the particle is set free beyond a certain location. It is clear that the total increase of drag due to stratification can be accounted for by the buoyancy force exerted by the caudal fluid column, at least until the maximum drag coefficient is attained. This implies that C_{ID} does not play a major role in increasing the drag when the caudal fluid is attached to the particle.

As the particle descends deep into the stratified layer (i.e. large $(z - z_{int})/d_p$), the dye streaks marking the envelope of the caudal fluid column faded and its coordinates could not be located accurately using the digital image processing technique employed. Thus, the data based on (3.15) are depicted in figure 16 only up to a certain $(z - z_{int})/d_p$. In addition, the caudal fluid column is unsteady and is subjected to viscous friction at the periphery, which should be accounted for in a rigorous analysis. Such effects cannot be delineated by the limited capabilities of the experimental techniques used in our study.

4. Conclusions and discussion

An experimental study aimed at understanding flow phenomena associated with particle settling in density-stratified fluids is described in this paper. The flow con-

figuration consisted of a three-layer stably stratified fluid, with the upper and lower homogeneous layers separated by a density interface of thickness δ and buoyancy frequency N. Individual particles of diameter $d_p \ll \delta$ were released into the top layer; they first accelerated, achieved a steady settling velocity U_1 and then entered the density-stratified region. Digital particle tracking was used to obtain the instantaneous velocity and acceleration of particles, using which the drag exerted on individual particles was calculated based on an approximate equation of motion. The efficacy of this methodology was established by evaluating the drag coefficient of solid particles settling in homogeneous fluids and comparing it with previous drag measurements.

It was found that in the Reynolds number $Re_1 = U_1 d_p/\nu$ regime $1.5 < Re_1 < 15$ the effect of stratification on particle settling is significant, in that the drag on a particle increased sharply upon entry into the stratified layer. As a result, the particle decelerated to a minimum velocity U_{min} and thereafter accelerated back to the local settling velocity. In the limited Froude number $Fr_1 = U_1/Nd_p$ range investigated, $3 < Fr_1 < 10$, the Reynolds number range for enhanced drag appeared to be insensitive to Fr_1. The minimum velocity of the particle was given by $U_{min}/U_1 = 5.5 \times 10^{-2} Fr_1^{9/10}$, which is achieved after it travelled for a time of $t_{min}/(d_p^2/\nu) = 1.4 \times 10^2 Re_1^{-1.7}$ within the stratified layer.

Detailed visualization of flow around a settling particle revealed that the increase of drag on the particle occurred due to the dragging of a lighter fluid column attached to the particle, from the upper layer into the stratified layer. The buoyancy force acting on this caudal fluid column is transmitted to the particle as a drag force F_{SD}, in addition to other drag forces on the particle. The drag due to the drawing down of upper-layer fluid could account for the entire increase of drag due to the presence of stratification, at least up to the instant where maximum drag occurs. The internal wave drag was found to be negligible compared to the drag due to caudal fluid. The internal waves, however, were excited in the interface after the particle detached from the caudal fluid column; the potential energy associated with the fluid column was released as internal wave energy, as the fluid column retracted back to the neutral buoyancy level.

The formation of tailing fluid columns behind solid bodies (Lin *et al.* 1992) and slowly rising bubbles (Bush & Eames 1998) has been reported before, but their implication for drag enhancement has not been investigated in the context of stratified flows. As a particle rises, the no-slip boundary condition causes the fluid to drag along, which is countered by the viscous and buoyancy forces associated with the dragged fluid column. In the absence of buoyancy forces (i.e. particles in the upper layer), the length L of the dragged fluid column is determined by a balance between viscous ($\nu U/d_p^2$) and inertial forces (U^2/L) of the column, leading to a caudal fluid column length of $L \sim d_p Re$. Of course, this is possible only in a limited Re range where such a balance can be established. As the particle enters the stratified layer, this tailing fluid having the density of the upper layer is drawn behind, and the particle immediately feels a buoyancy force. This buoyancy force increases as the particle descends, soon becoming strong enough to break down the caudal fluid column due to the change of force balance (when the buoyancy force exceeds the inertia force). The subsequent motion is expected to be dependent on the prevailing Reynolds number, and it is possible that another caudal fluid column develops following the breakup of a tail. In the present experiments, however, the particles enter the bottom homogeneous layer shortly after the first breakup, and hence detailed observations of the subsequent motion could not be made.

Finally, it is of interest to comment on the drag characteristics of a particle having a Reynolds number that lies outside the range $1.5 < Re_1 < 15$. Experiments at higher Re_1 carried out with heavier particles showed no significant change of drag coefficient as they passed through the interface, with the total drag coefficient being approximately the same as that observed in homogeneous fluids. Experiments carried out with small particles at low Re_1 also showed continuous adjustment of the particle velocity to the background variation of density, and the drag coefficient coincided with its homogeneous fluid counterpart.

It is instructive to discuss the application of above results to atmospheric and oceanic situations. MacIntyre *et al.* (1995) considered the settling of marine snow through the upper oceanic stratified layers of different buoyancy frequencies. They identified settling of aggregates with diameter 0.5–10 mm at speeds of 35–200 m day^{-1} through regions with $N \approx 0.011$ s^{-1} (moderate stratification), $N \approx 0.016$ s^{-1} (strong stratification) and $N \approx 0.039$ s^{-1} (maximum stratification). The Reynolds numbers of descent are within the range 0.2–23 and the Froude numbers for the three stratification types are 20–70, 14–50 and 5–20, respectively. Thus, it is expected that the descent of marine snow in oceans can be strongly influenced by the stratification drag.

The conditions prevailing in the lower atmosphere are different. The data taken during the Phoenix Air Flow Experiment (PAFEX-1) conducted during Jan 14–Feb 4, 1998 in the metropolitan Phoenix area revealed a mean particle size of $d_p = 1$ μm dispersed in the morning stably stratified boundary layer of $N \approx 0.06$ s^{-1}. The corresponding values are $Re \approx 10^{-5}$ and $Fr \approx 10^4$, indicating that the stratification drag is unimportant for airborne particles in this particular urban boundary layer. It appears that this inference is generally valid for nocturnal boundary layers under normal urban conditions laden with secondary aerosols (which are particles in fine size ranges formed by chemical conversions in the atmosphere). On the other hand, the atmospheric boundary layer can also carry the so-called primary aerosols consisting of soil and dust formed by the physical breakup of material at Earth's surface (Fennely 1981) or by industrial emissions. These aerosols have typical diameters on the order 100 μm. Taking typical values of $N \approx 0.06$ s^{-1} in the inversion layers and $\rho_p \approx 2400$ kg m^{-3}, it is possible to obtain $Re \approx 10$ and $Fr \approx 10^5$ which suggest possible development of tailing fluid columns behind such aerosols.

To our knowledge, this is the first laboratory investigation on the settling of particles through density-stratified layers. The present study also contrasts with numerous studies carried out on the horizontal movement of bluff objects in stratified fluids (Foster & Saffman 1970; Lofquist & Purtell 1984; Gorodotsov 1992; Lin *et al.* 1992). Theoretical studies on inviscid flow around bodies moving in weakly stratified fluids with insignificant buoyancy effects have been revived by Eames & Hunt (1997), and it is hoped that the present investigation will inspire further theoretical and experimental studies on the settling of a single particle or a swarm of particles in stratified fluids at low and moderate Reynolds number.

The authors wish to thank Professor Karl Sieradzki and Mr Stanko R. Branković who generously provided access to the facilities of the STM/Mechanics and Growth of Thin Films Laboratory. The funding for the research reported herein was provided by the Environmental Protection Agency (Office of Exploratory Research) and the National Science Foundation (Environmental Geochemistry and Biogeochemistry Initiative; Fluid Mechanics and Hydraulics Program). The stratified and rotating flow research at Arizona State University is also funded by the Army Research Office and the Office of Naval Research.

REFERENCES

Benjamin, T. B. 1986 Note on added mass and drift. *J. Fluid Mech.* **169**, 251–256.

Berdan, C. & Leal, L. G. 1982 Motion of the sphere in the presence of deformable interface. Part 3. Numerical study of the translation of a sphere parallel to an interface. *J. Colloid Interface Sci.* **87**, 62–80.

Bush, J. W. M. & Eames, I. 1998 Fluid displacement by high Reynolds number bubble motion in a thin gap. *Intl J. Multiphase Flow* **24**, 411–430.

Clift, R., Grace, J. R. & Weber, M. E. 1978 *Bubbles, Drops and Particles*. Academic.

Dalziel, S. B. 1992 Decay of rotating turbulence: some particle tracking experiments. *Appl. Sci. Res.* **49**, 217–244.

Dalziel, S. B. 1993 Rayleigh-Taylor instability: experiments with image analysis. *Dyn. Atmos. Ocean.* **20**, 127–153.

Darwin, C. 1953 Note on hydrodynamics. *Proc. Camb. Phil. Soc.* **49**, 342–354.

Drayton, M. J. 1993 Eulerian and Lagrangian studies of inhomogeneous turbulence generated by an oscillating grid. PhD thesis, DAMTP, Cambridge University.

Eames, I., Belcher, S. E. & Hunt, J. C. R. 1994 Drift, partial drift and Darwin's proposition. *J. Fluid Mech.* **275**, 201–223.

Eames, I. & Hunt, J. C. R. 1997 Inviscid flow around bodies moving in weak density gradients without buoyancy effects. *J. Fluid Mech.* **353**, 331–355.

Eames, I., Hunt, J. C. R. & Belcher, S. E. 1996 Displacement of inviscid fluid by a sphere moving away from a wall. *J. Fluid Mech.* **324**, 333–353.

Fennely, P. F. 1981 The origin and influence of airborne particulates. In *Climates, Past and Present* (ed. B. J. Skinner). Kauffmann.

Foster, M. R. & Saffman, P. G. 1970 The drag of a body moving transversely in a confined stratified fluid. *J. Fluid Mech.* **43**, 407–418.

Geller, A. S., Lee, S. H. & Leal, L. G. 1986 The creeping motion of spherical particles normal to a deformable interface. *J. Fluid Mech.* **169**, 27–69.

Gorodotsov, V. A. 1992 Behaviour of sphere in an ideal, uniformly stratified medium. *Fluid Mech. Res.* **21**(6), 100–106.

Hartland, S. 1968 The profile of draining film between a rigid sphere and a deformable fluid-liquid interface. *Chem. Engng Sci.* **24**, 987–995.

Huppert, H. E., Turner, J. S. & Hallworth, M. A. 1995 Sedimentation and entrainment in dense layers of suspended particles stirred by an oscillating grid. *J. Fluid Mech.* **289**, 263–292.

Jones, A. F. & Willson, S. D. R. 1978 The film drainage problem in droplet coalescence. *J. Fluid Mech.* **87**, 263–288.

Kadanoff, L. P. 1997 Singularities and blowups. *Physics Today*, September 1997, 11–13.

Kellog, W. N. 1990 Aerosols and climate. In *Interaction of Energy and Climate* (ed. W. Bach, J. Pankrath & J. Williams). Reidel.

Lande, R. & Wood, A. M. 1987 Suspension times of particles in the upper ocean. *Deep-Sea Res.* **34**, 61–72.

Larsen, L. H. 1969 Oscillations of a neutrally buoyant sphere in a stratified fluid. *Deep-Sea Res.* **16**, 587–603.

Lee, S. H., Chadwick, R. S. & Leal, L. G. 1979 Motion of a sphere in the presence of a plane interface. Part 1. An approximate solution by generalization of the method of Lorentz. *J. Fluid Mech.* **93**, 705–726.

Lee, S. H. & Leal, L. G. 1982 Motion of a sphere in the presence of a deformable interface. Part 2. Numerical study of the translation of sphere normal to interface. *J. Colloid and Interface Sci.* **87**, 81–106.

Lighthill, M. J. 1956 Drift. *J. Fluid Mech.* **1**, 31–53.

Lighthill, M. J. 1996 Internal waves and related initial value problems. *Dyn. Atmos Ocean.* **23**, 3–17.

Lin, Q., Lindberg, W. R., Boyer, D. L. & Fernando, H. J. S. 1992 Stratified flow past a sphere. *J. Fluid Mech.* **240**, 315–355.

Lofquist, K. & Purtell, P. 1984 Drag on sphere moving horizontally through a stratified liquid. *J. Fluid Mech.* **148**, 271–284.

MacIntyre, S., Alldredge, A. L. & Gotschalk, C. C. 1995 Accumulation of marine snow at density discontinuities in the water column. *Limnol. Oceanogr.* **40**, 449–468.

Magnaudet, J. J. M. 1997 The forces acting on bubbles and rigid particles. *ASME Fluids Engineering Division Summer Meeting, Vancouver, British Columbia.*

Maru, H. C., Wasan, T. D. & Kintner, R. C. 1971 Behaviour of a rigid sphere at a liquid interface. *Chem. Engng Sci.* **26**, 1615–1628.

Mowbray, D. E. & Rarity, B. S. 1967 The internal wave pattern produced by a sphere moving vertically in a density stratified liquid. *J. Fluid Mech.* **30**, 489–495.

Nikiforovich, Y. I. & Dudchak, K. P. 1992 Fall of a rigid thermally-conducting sphere through a thermally stratified fluid. *Fluid Mech. Res.* **21**, 7–14.

Odar, F. & Hamilton, W. S. 1963 Forces on a sphere accelerating in a viscous fluid. *J. Fluid Mech.* **18**, 302–314.

Perera, M. J. A., Fernando, H. J. S. & Boyer, D. L. 1994 Turbulent mixing at an inversion layer. *J. Fluid Mech.* **267**, 257–298.

Princen, H. M. & Mason, S. G. 1965 Shape of fluid drop at fluid/liquid interface. ii theory for three phase systems. *J. Colloid Sci.* **65**, 246–266.

Shah, S. T., Wasan, D. T. & Kintner, R. C. 1972 Passage of a liquid drop through a liquid-liquid interface. *Chem. Engng Sci.* **27**, 881.

Shopov, P. J. & Minev, P. D. 1992 The unsteady motion of the bubble or drop towards a liquid-liquid interface. *J. Fluid Mech.* **235**, 123–141.

Smith, P. G. & Van De Ven, T. G. M. 1984 The effect of gravity on the drainage of thin liquid film between a solid sphere and a liquid–fluid interface. *J. Colloid Interface Sci.* **100**, 456–464.

Thornham, S. A. & Wilson, D. R. 1983 The settling of a porous body through a density interface. *J. Fluid Mech.* **126**, 369–378.

Turco, R. P., Toon, O. B., Ackerman, T. P. & Pollack, J. B. 1993 Nuclear winter: Global consequence of multiple nuclear explosions. *Science* **222**, 1283–1292.

Warren, F. M. G. 1960 Wave resistance to vertical motion in stratified fluid. *J. Fluid Mech.* **7**, 209–229.

White, F. M. 1991 *Viscous Fluid Flow*. McGraw–Hill.

Yih, C. S. 1985 New derivations of Darwin's theorem. *J. Fluid Mech.* **152**, 163–172.